Additive Manufacturing 36 (2020) 101494

Contents lists available at ScienceDirect

Additive Manufacturing

journal homepage: www.elsevier.com/locate/addma

Productivity optimization of laser powder bed fusion by hot isostatic pressing

Dirk Herzog[a,b,*], Katharina Bartsch[a,b], Bastian Bossen[a]

[a] Institute of Laser and Systems Technology, Hamburg University of Technology, Denickestr. 17, 21073 Hamburg, Germany
[b] Fraunhofer Research Institution for Additive Manufacturing Technologies IAPT, Am Schleusengraben 14, 21029 Hamburg, Germany

ARTICLE INFO

Keywords:
L-PBF
SLM
Hot isostatic pressing
Productivity
Process optimization
Ti-6Al-4V

ABSTRACT

Laser Powder Bed Fusion is today used for the serial production of parts, e.g. in the medical and aerospace markets. One of the major limitations is the comparatively low build rate of the process, which leads to low productivity and high costs when compared to conventional processes. Current approaches such as the use of multi-laser systems help increasing the build rate but come at higher investment costs. Overall, the low productivity limits the number of business cases for Laser Powder Bed Fusion and hinders the market uptake in more cost-sensitive industries.

This paper suggests a combined approach of Laser Powder Bed Fusion and subsequent Hot Isostatic Pressing as a method to improve productivity. Hot Isostatic Pressing is often used as a post-process to eliminate any remnant porosity. It is shown that the process, however, is able to densify specimens that come out of Laser Powder Bed Fusion with an as-build density as low as 95 %. This opens up a larger process window for the initial Laser Powder Bed Fusion step. Experimental investigations are presented using two commercial Laser Powder Bed Fusion systems with the widely used titanium alloy Ti-6Al-4V. Instead of optimizing the process for the highest possible density, the parameters were optimized to yield the highest possible speed while maintaining a density above 95 %. A scan speed increase of 67 % was achieved and the specimens were then successfully compacted to above 99.8 % density in the Hot Isostatic Processing step. The high-speed parameter set was then applied to a demonstrator build job, where it leads to an overall saving of 26 % of build time.

This research did not receive any specific grant from funding agencies in the public, commercial, or not-for-profit sectors.

1. Introduction

Laser Powder Bed Fusion (L-PBF) is a process widely used for Additive Manufacturing (AM) of complex metallic parts in industrial applications [1]. From the many existing AM processes, L-PBF offers a high part quality and accuracy [2] that enables process qualification in industrial sectors with high standards such as medical or aerospace [3].

On the downside, L-PBF features relatively low productivity in terms of build rates between 2 and 40 cm^3/h (especially depending on material) [4].

The build rate in L-PBF is defined as the product of layer thickness l, hatch distance h and scan speed v [5]:

$$V = l * h * v \tag{1}$$

Thus, it can be derived from (1) that the build rate may in general be increased by either increasing layer thickness, or hatch distance, or scan speed, or by a combination of these parameters. However, to yield dense specimens, the energy input has to be sufficient to melt the whole volume element. In literature, the volume energy E_V is typically used to describe the energy input in L-PBF, which is defined as [1]:

$$E_V = P_L / (l * h * v) = P_L / V \tag{2}$$

with P_L = laser power. For the titanium alloy Ti-6Al-4V, achievable build rates reported in the literature range from 18 cm^3/h (30 µm layer thickness) [6] to 32 cm^3/h (60 µm layer thickness) [7] when a standard single laser machine with $P_{L,max}$ = 400 W is used. Shi et al. [8] have shown that for Ti-6Al-4V, the build rate can be increased, if e.g. the layer thickness is raised to l = 200 µm while adjusting the hatch spacing, scan speed and laser power at the same time, in order to maintain a density of ρ > 99.73 %. The higher laser power needed, however, produced higher spatter due to higher recoil pressure and an increase in surface roughness. Higher layer thicknesses also decrease part accuracy

* Corresponding author.
E-mail address: dirk.herzog@tuhh.de (D. Herzog).

https://doi.org/10.1016/j.addma.2020.101494
Received 16 April 2020; Received in revised form 21 July 2020; Accepted 29 July 2020
Available online 05 August 2020

in build direction due to a more significant staircase effect [9]. As such, there is a trade-off between productivity on the one hand, and surface roughness and tolerances on the other hand. The layer thickness is therefore typically chosen between l = 25 µm and l = 60 µm [10].

The low productivity is a major limitation for an economical application of L-PBF to a broad range of industrial use-cases [11], especially if serial production with higher lot sizes is concerned. Therefore, methods and approaches to improve the productivity of L-PBF are a key area of research. Examples of approaches to increase build rate that were adapted in commercial L-PBF systems include e.g. the skin-core technology [12] and the multi-laser approach [5]. The skin-core technology uses different spot sizes and parameters for the laser exposure of the skin (or contour) of the part, and the core (or volume) [13]. While the contour parameters are optimized for quality and accuracy, the volume parameters are optimized for productivity [4]. Poprawe et al. [14] showed that an increase in theoretical build rate by a factor of 8.9 was possible, when the core was exposed using a higher layer thickness than for the skin, i.e. by only exposing the core every fifth layer, and increasing the laser power to P_L = 2 kW (in comparison to P_L = 300 W used as reference, for tool steel 1.2709). The multi-laser approach uses a set-up of typically two or four lasers directed through one scanner each, and working in parallel in the same powder bed. The exposure step can therefore be accelerated by a factor correlating to the number of lasers used [15]. The overall productivity of a common 4-laser L-PBF system for parts out of Ti-6Al-4V reaches a value of 105 cm^3/h [4]. Kopf et al. [16] developed a cost-model that would propose a 27 × 1 kW laser system being optimal and would reduce the production costs by 43 % compared to a 2 × 700 W system used as a reference. It should be noted that both technological approaches need a major modification of the machine layout.

The titanium alloy Ti-6Al-4V (also referred to as Grade 5) is the most common titanium alloy in industrial applications [17]. It is an α-β-alloy with superior mechanical performance (Yield strength YS = 860 MPa, Ultimate Tensile Strength UTS = 930 MPa, Elongation at break ε_B > 10 %; according to ASTM F1472, in wrought condition) and high corrosion resistance. It has also been the material of choice for L-PBF of many medical and aerospace applications such as hip implants [18] or brackets and fuel system parts [1]. In L-PBF, Ti-6Al-4V is known to form a lamellar, basket-weave microstructure consisting mostly of the martensitic α'-phase [19]. The resulting mechanical properties in the as-build condition are governed by comparably high strength but reduced ductility [20,21]. The microstructure, and thus also the properties, may show a pronounced anisotropy due to different cooling conditions in the build direction and perpendicular to it [19]. The large and directional thermal gradients in L-PBF also result in residual stresses [22,23]. Therefore, Ti-6Al-4V parts manufactured by L-PBF are typically heat-treated for stress-relieve, as well as to transfer the α'-phase into a more ductile and isotropic α + β microstructure [24,25].

In L-PBF, various process parameters such as scan speed and strategy, laser power, hatch distance, layer thickness, and spot size determine the local energy distribution [26]. Thomas et al. [27] have shown that a processing diagram using a normalized energy density E* as the abscissa and the inverse value of a normalized hatch spacing h* as the ordinate may be used to predict specimen density. The normalized values may be calculated by the following terms:

$$E^* = A^* P_L / (2^* v^* l^* r_b^* \rho^* c_p^* (T_m - T_0)) \quad (3)$$

$$h^* = h / r_b \quad (4)$$

with A = absorptivity of the material for the laser wavelength, c_p = specific heat capacity, T_m = melting temperature, T_0 = initial temperature, and r_b = beam radius (in the work plane). In simplified terms, E* thus represents the energy input into a volume element with respect to the minimum energy needed to melt this volume element, and may therefore be used for any material by applying the thermo-physical properties of the material. Three areas can be defined in such a processing map: combinations of E* and 1/h* resulting in lack of fusion pores from incomplete melting, combinations of E* and 1/h* yielding high-density (e.g. ≥ 99.5 %) specimens and thus define the process window, and combinations of E* and 1/h* resulting in entrapped gas pores from evaporation. Regularly, process parameters are optimized for maximum density of 99.5 % or higher [28]. The maximum productivity will then be achieved for a given laser power at a corresponding maximum scan speed still inside the processing window, and just avoiding lack of fusion pores. Lack of fusion pores are known to be specifically detrimental to fatigue life of L-PBF parts, as their irregular shape may act as a crack initiation site inside the material, and are thus avoided [29].

To close any remnant porosity in fatigue-critical parts, Hot Isostatic Pressing (HIP) may be used [30]. In HIP, parts are subject to a combination of elevated temperature and pressure for a defined period. The temperature is chosen to reduce the yield strength to below the gas pressure, thus allowing for plastic flow [31]. The high pressure results in substantial shrinkage of closed pores, and they are either completely eliminated or at least reduced in size to below the detection limit of the typical analyzing technologies such as scanning electron microscopy (SEM). As an effect, HIP treatment improves the fatigue behavior of L-PBF parts [32]. HIP parameters for L-PBF of Ti-6Al-4V are designed to stay below β-transus temperature of 995 °C [17] and use a high pressure to reduce the porosity effectively while keeping grain growth limited. Typically, the material is subjected to a temperature of T = 920 °C at a pressure of p = 100 MPa for a duration of 2 h under argon atmosphere [33], which will also transfer the lamellar as-build α'-microstructure to a more globular α + β. Generally, parts with a density of ρ > 90 % are known to feature mainly closed pores and thus can be completely compacted using HIP [34]. With higher HIP pressures of p = 200 MPa possible today, the temperature needed to achieve full densification may be lowered to T = 820 °C, which may improve tensile strength [35]. HIP is also used to compact pre-sintered powders [36], where the problem of open porosity is overcome by encapsulation or coating [34]. Das et al. [37] have already proposed a process combination of L-PBF and HIP in 1996, when L-PBF was comparatively immature and still struggling to produce parts of high density. In their approach, L-PBF is used to generate the outer structure or shell of a part and leaving the interior with unmelted powder. Afterward, the part is evacuated and sealed, and then compacted by HIP. Qiu et al. [38] have recently re-assessed this shelling approach for Ti-6Al-4V and found that it may be used to produce fully dense parts. Cai et al. [39] have confirmed this, while also showing that the specimens produced failed in the L-PBF-side rather than in the compacted-powder or interface area during fatigue testing. The high amount of shrinkage currently limits this route to the production of simple axis-symmetrical components, for which the final shape can be predicted by modeling [38].

This paper suggests combining L-PBF and HIP in a similar way with the primary goal to increase the productivity of the L-PBF process. Instead of optimizing the L-PBF parameters for maximum density, the approach presented here consists of a scan-speed optimization during L-PBF while maintaining the density above 95 % to safely exclude open porosity, and subsequently compacting the material in a HIP process to density values above 99.8 %. Compared to the shelling approach discussed above, the overall porosity is kept much lower and with a homogenous distribution, thus allowing for unidirectional compaction in HIP and control of the final part shape.

2. Materials and methods

The general approach of this study consists of two steps. Firstly, data sets from two different L-PBF systems are evaluated and compiled to a process map with the goal to provide the reader with a process window for the L-PBF process independent from the machine used. Secondly, high-speed parameters are developed with the goal to achieve high productivity, and achieving full density only after HIP. The specimens

Table 1
Process parameter range for the process map and high-speed investigations.

L-PBF system			EOS M290	SLM 500 HL	
parameter		unit	process map	process map	high-speed
laser power	P_L	W	280–370	200–260	240–380
scan speed	v	m/s	1.1–1.6	0.7–1.2	1.4–3.4
hatch	h	µm	100–190	105	87–145
temperature of powder bed	T_0	K	473.15		
layer thickness	l	µm	60		

from the high-speed investigations are then evaluated for as-build density, and selected samples are analyzed regarding their microstructural development and residual stresses. Selected specimens are HIP-treated to derive the density after HIP, and to conclude the process window for the combined L-PBF plus HIP process, in comparison to L-PBF only.

For the high-speed parameter investigations, a commercial L-PBF system of the type SLM 500 H L (SLM Solutions Group AG, Lübeck, Germany) was used. The machine has a build envelope of 500 × 280 × 365 mm^3 and is equipped with 4 lasers of a maximum laser power of $P_{L,max}$ = 400 W each. To enhance the data base for the processing diagram, specimens produced on another commercial L-PBF system, type EOS M290 (EOS GmbH, Krailing, Germany), were also used. This system features a build envelope of 250 × 250 × 325 mm^3 and is equipped with one laser of a maximum laser power of $P_{L,max}$ = 400 W. Table 1 shows the parameter range of all specimens included in this study for the process map, as well as the range in which the parameters were varied to find high-speed parameters. The layer thickness was chosen at l = 60 µm as a compromise between the desired high productivity and acceptable accuracy.

For the construction of the processing diagrams, the focal radius is needed. It has to be noted, that the data for these diagrams has been collected over a long period of time of approx. 3 years. Therefore, the radius was calculated from the last available beam propagation measurements and was found to be r_{SLM500} = 43.6 µm and r_{EOS290} = 49.3 µm (measured at 50 % of maximum laser power each). The thermophysical properties for the alloy Ti-6Al-4V used to calculate the normalized energy densities are provided in Table 2.

The powder used for the high-speed parameter investigations was a Ti-6Al-4V (Grade 23) powder manufactured by induction-coupled plasma atomization (Tekna Advanced Materials Inc., Sherbrooke, Canada). The particle size distribution of the powder was 15–45 µm. The specimens evaluated for the processing diagram were manufactured with a number of different Ti-6Al-4V powders and suppliers over the course of time.

Two types of specimens were manufactured for the investigations. Density cubes of a size of 10 × 10 × 10 mm^3 were used to evaluate the influence of build parameters on the density and microstructure in the as-build and HIPed conditions. To evaluate the density, cross-sections were prepared out of the specimens, ground and polished using an oxide polishing suspension. Micrographs from the x–z plane of the specimens (coordinate system according to EN ISO/ASTM 52921:2016) were then analyzed using light microscopy (Olympus GX51, Olympus Europa SE & Co. KG, Hamburg, Germany) and the porosity was calculated using image analysis software (ImageJ, public domain) based on ISO 4499-4:2016. This method was chosen because it offers - in contrast to the Archimedes method - the possibility to analyze pore distribution, pore geometry and microstructure from the same micrographs. Also, Archimedes method cannot be used when open porosity is present, which can be expected for some of the samples in this investigation. Density analysis per micrographs is known to yield results with high accuracy for densities above 98 % [44], while for densities down to 95 % the variance may increase to 1–2 percentage points.The microstructure was analyzed using SEM (Zeiss Supra 55VP, Carl Zeiss Microscopy GmbH, Jena, Germany).

A selection of density cubes with varying as-build densities between ρ = 99.30 to 93.45 % was HIP-treated at a temperature of T = 820 °C and a pressure of p = 200 MPa for 2 h. The as-build density was analyzed from separate specimens build on the same build job as the ones sent to HIP. The HIP treatment was performed at Quintus Technologies Application Centre (Västerås, Sweden).

For the qualitative comparison of residual stresses, a twin cantilever beam geometry was used as described in [40], with a size of 800 × 70 × 70 mm^3 (length × width × height), and the free length of each arm was 365 mm. The cantilever beam specimens were placed on the build platform in a way that the whole geometry was built by one individual laser to avoid any effects of overlapping between scan fields. The as-build cantilevers were then wire-eroded from the build plate, and the deflection of the cantilever arms was measured.

Table 2
Thermophysical properties of Ti-6Al-4V and characteristics of the set-up.

property		unit	value	reference
absorptivity	A	–	0.4	[40]
specific heat capacity	c_p	J/gK	0.5263	[26]
solidus temperature	T_{Sol}	K	1878	[41]
liquidus temperature	T_{Liq}	K	1928*	[41]
heat of fusion	H	J/g	290	[42]
density	ρ	g/cm^3	4.43	[43]

* mean value taken from [41].

3. Results

3.1. Process map for Ti-6Al-4V

In order to derive the process window for Ti-6Al-4V, a total of 81 data sets from the two L-PBF systems with varying process parameters within the limits given in Table 1 were analyzed for their densities, and the normalized energy density E* and normalized hatch h* was calculated for each specimen. The governing idea behind the normalized energy density is to divide the actual energy input by the minimum energy input needed to completely melt a volume element. Therefore, Eq. 3 was modified by using the solidus temperature T_{Sol} of the alloy, and in addition the heat of fusion H was added to acquaint for the energy input needed to transfer the alloy to the liquidus temperature T_{Liq}, resulting in Eq. 5. Here, the heat of fusion contributes to the term by approximately 38 %, thus the amount needed to melt the volume element would otherwise be underestimated.

$$E^* = A^* P_L / (2^*v^*l^*r_b^*\rho^*c_p^*(T_{Sol}-T_0)+H) \quad (5)$$

The data was then plotted as a process map by sorting the values according to density ranges, as given inFig. 1 . In general, low values of E* will result in lack of fusion pores, while comparatively high values of E* will result in gas pores. The process window resulting in high density specimens (> 99.5 %, dark green in Fig. 1) is situated between these two areas. The data also shows that the width of the process window is depending on 1/h*, i.e. for a 1/h* = 0.42, high density specimens will be achieved for 2.89 ≤ E* ≤ 4.15, while for 1/h* = 0.26 this is only true for 3.92 ≤ E* ≤ 4.22. Still, the lower 1/h* value would yield higher productivity, as avoiding the lack of fusion area would require an increase of 35 % in E* (e.g. by reducing the scan speed) but at the same time, the hatch could be increased by almost 62 %. A trade-off between higher productivity of the L-PBF process at lower 1/h* and higher robustness at higher 1/h* values is obvious.

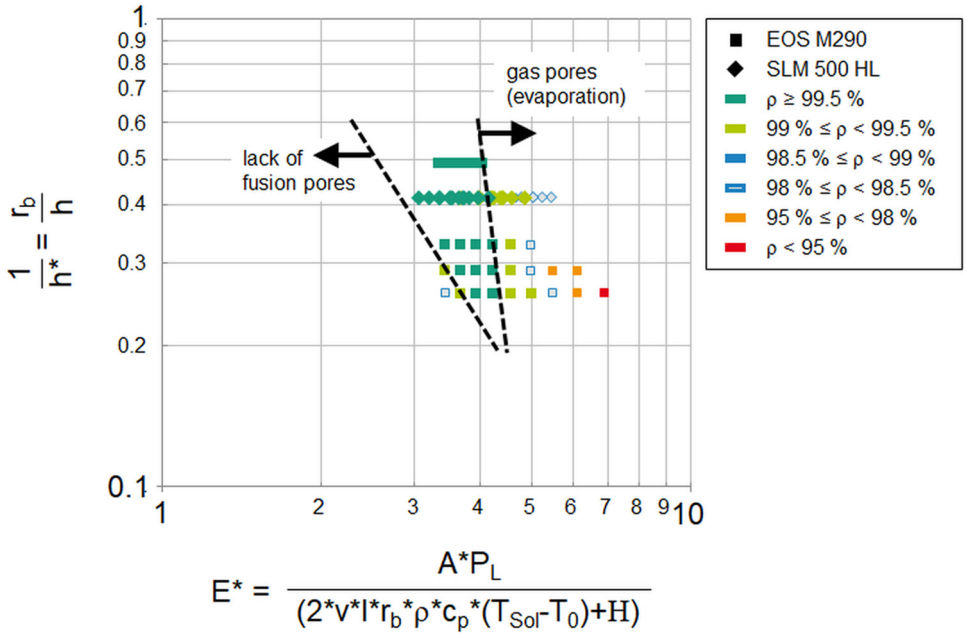

Fig. 1. Process map for Ti-6Al-4V based on 81 data sets with varying process parameters from two different commercial L-PBF systems (For interpretation of the references to colour in this figure legend, the reader is referred to the web version of this article.).

3.2. Density evolution with high-speed parameters

Usually, parameters resulting in lack of fusion pores are avoided. Thus, only limited data is available for the resulting densities if E* is further reduced. For the combination of L-PBF and HIP suggested in this paper, however, it is necessary to know the process window achieving densities down to ρ = 95 %. To exploit this area, experiments have been conducted at three different fixed levels of 1/h* (0.5, 0.42 and 0.3), and E* has been lowered by increasing the scan speed. The corresponding micrographs are displayed in Figs. 2, 3 and 4, , .

For the highest 1/h* (1/h* = 0.5, corresponding to the smallest hatch, cf. Fig. 2) and starting with a reference parameter set yielding close to full density (ρ = 99.98 %, E* = 3.35, v = 1.2 m/s), the density does not change significantly if the scan speed is increased to 116 % with respect to the reference (ρ = 99.97 %, E* = 2.87) and further to 133 % (ρ = 99.95 %, E* = 2.51). The first irregular-shaped, smaller pores appear at this value. When the scan speed is further increased to 150 % (ρ = 99.84 %, E* = 2.24) and on to 167 % (ρ = 99.54 %, E* = 2.01), there is evidently an increasing number of irregular-shaped (lack of fusion) pores while the overall density stays comparatively high. This effect may be mainly due to the still comparatively small pore sizes in the range of 80 µm (in the major axis). Increasing the speed to 183 % (ρ = 98.14 %, E* = 1.83), the overall density drops significantly as the number of lack of fusion pores increases, and the size of

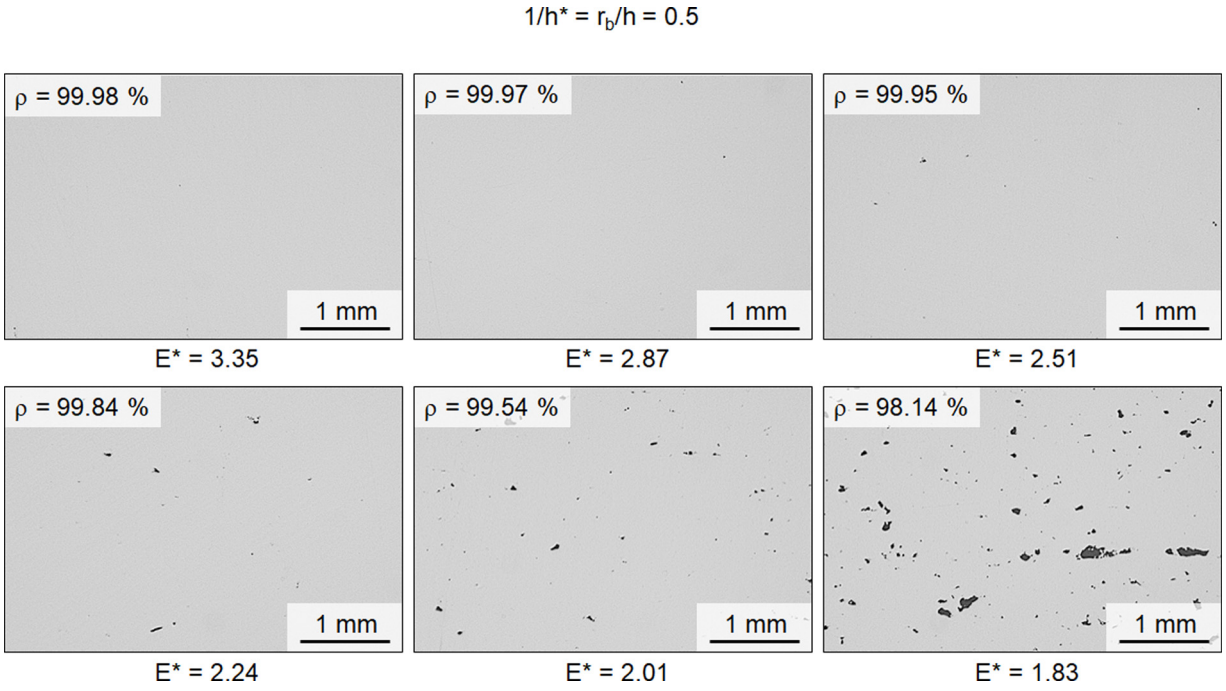

Fig. 2. Micrographs of specimens for a constant 1/h* = 0.5 and with lower E* from top left to bottom right.

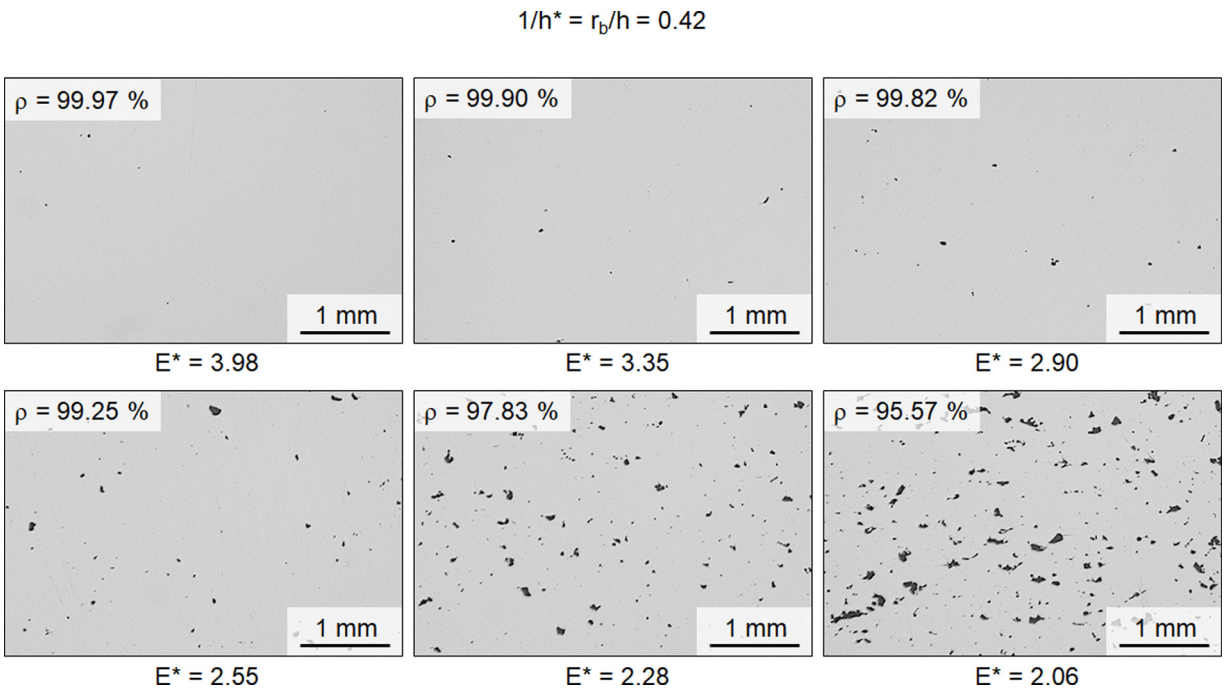

Fig. 3. Micrographs of specimens for a constant 1/h* = 0.42 and with lower E* from top left to bottom right.

the largest pores jumps to > 500 µm.

A similar tendency can be observed for 1/h* = 0.42 (cf. Fig. 3). Here, the reference value yielded a density of ρ = 99.97 % at E* = 3.98 (v = 1.6 m/s). An increase in scan speed to 119 % (ρ = 99.90 %, E* = 3.35) and 138 % (ρ = 99.82 %, E* = 2.90) leads to a rather marginal decrease in overall density, but the pore size already increases to > 60 µm at E* = 2.90. Further increase in scan speed leads to a more pronounced decline in density (156 %: ρ = 99.25 %, E* = 2.55; 175 %: ρ = 97.83 %, E* = 2.28; 194 %: ρ = 95.57 %, E* = 2.06). Again, the pore size increases disproportionately.

At the lowest 1/h* = 0.3, the same effect of declining density with increasing scan speed (lower E*) is observed. As expected from the process map (cf. Fig. 1), the width of the process window is smaller at high hatch and therefore the density declines faster. Considerably large pores (> 200 µm in major axis) are already observable at 150 % scan speed (ρ = 99.39 %, E* = 3.35, v = 0.8 m/s). At a scan speed of 200 % (E* = 2.51), the density reaches ρ = 94.2 % and thus falls below the threshold of 95 % (corresponding to expected full density after HIP). Interestingly, this also represents the first micrograph with large interconnected lack of fusion pores with up to 1 mm in length. These pores are oriented perpendicular to the build direction, indicating that most probably the energy input is not high enough to always melt the full layer thickness.

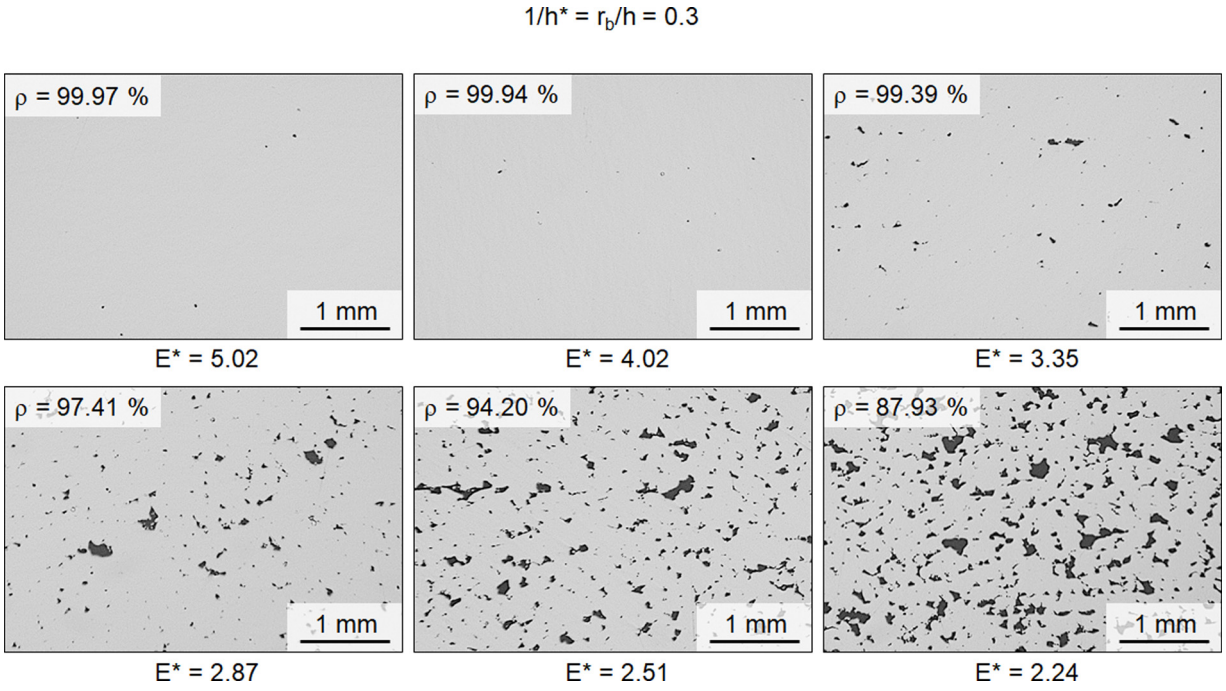

Fig. 4. Micrographs of specimens for a constant 1/h* = 0.3 and with lower E* from top left to bottom right.

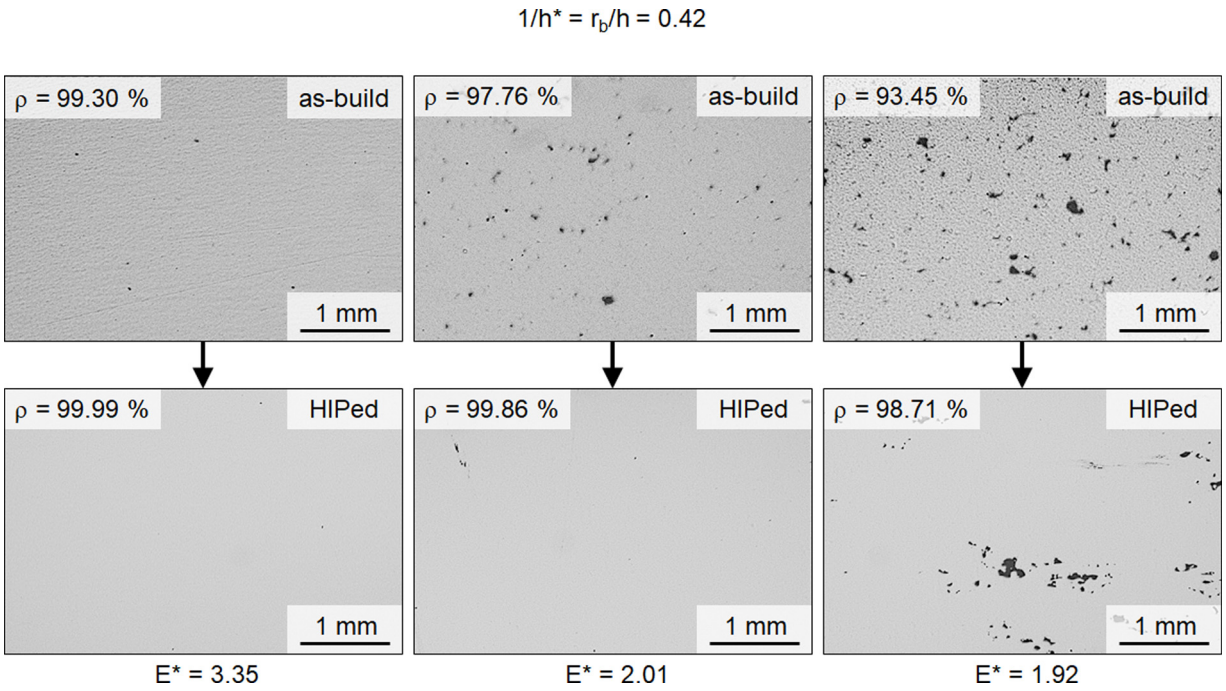

Fig. 5. Micrographs of as-build samples (top) and HIPed samples (bottom) originating from the same build job.

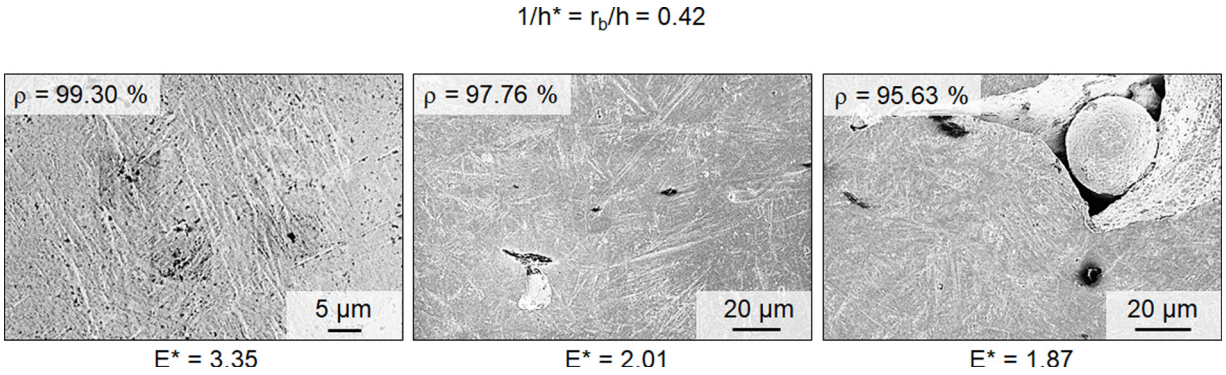

Fig. 6. Microstructure of as-build specimens. Reference parameter set (left) and high-speed specimens (center and right).

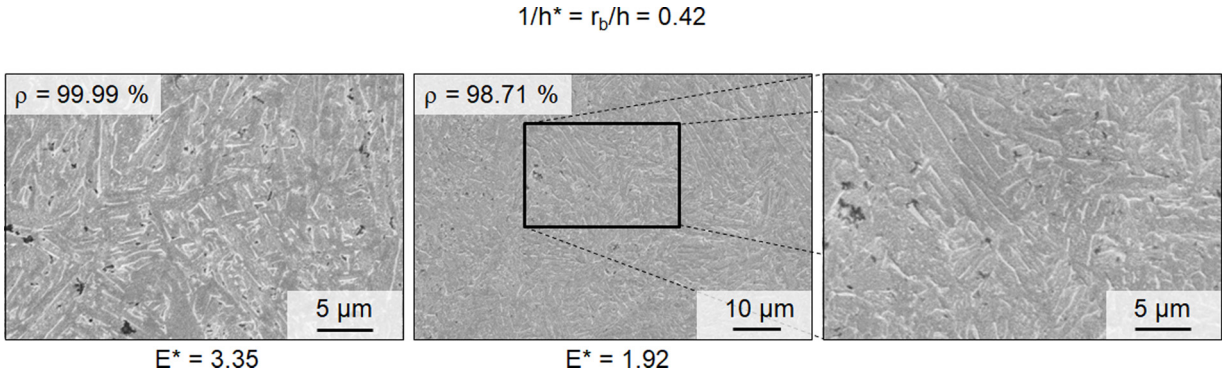

Fig. 7. Microstructure of specimens after HIP. Reference parameter set (left) and high-speed specimen (in overview, center; and in detail, right).

3.3. Hot isostatic pressing

For 1/h* = 0.42, several samples were HIP-treated as described in Section 2. The resulting density before and after HIP was again derived through micrographs, as shown in Fig. 5. Note that the as-build and HIPed samples were placed side-by-side on the same build job to exclude any other effects on density as much as possible. For the reference at E* = 3.35, the as-build density was ρ = 99.30 % and only a few smaller sized pores (in the range of 10 – 30 µm) were observed. In accordance with literature [30], further densification occurs in HIP to ρ = 99.99 %, cf. Fig. 5, left. Increasing the scan speed to 167 % (E* = 2.01), the as-build density expectedly drops to ρ = 97.76 %. Although not reaching full density, the HIP process proved to be effective in densifying the specimen to ρ = 99.86 %, and thus to the target area

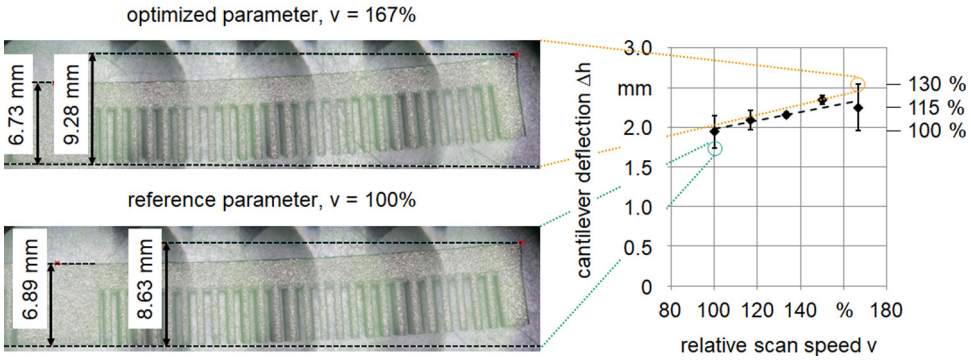

Fig. 8. Relative residual stresses (RS) as indicated by double cantilever beams, lowest RS reference parameter (bottom left) and highest RS speed-optimized parameter (top left).

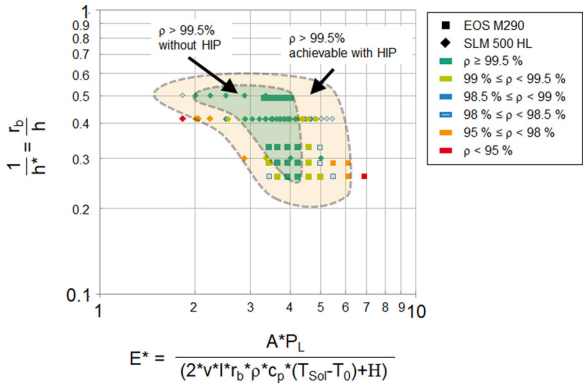

Fig. 9. Process map for Ti-6Al-4V with additional high-speed (low E*) values from section 3, showing the tentative process windows for which high density (ρ > 99.5 %) may be reached directly out of the L-PBF process (green-coloured area) and with a combination of L-PBF followed by HIP (light-yellow coloured area) (For interpretation of the references to colour in this figure legend, the reader is referred to the web version of this article.).

of ρ > 99.8 %, cf. Fig. 5, center.

Further increase in scan speed to 175 % (E* = 1.92) reduced the as-build density to ρ = 93.45 %. After HIP, the density can still be significantly increased to ρ = 98.71 %, but stays below the intended range. While the majority of the pores is at least compacted to below visibility in the micrographs, especially some of the larger pores persist. This confirms the hypothesis that HIP is especially effective for density values above ρ > 95 %.

3.4. Microstructure

The reference, as well as some selected high-speed specimens, have been further analyzed by SEM, before and after HIP. Fig. 6 shows the microstructure of as-build specimens. The microstructure consists of needle-like, mostly α 'microstructure, more or less independent from E*. Areas with unmolten powder particles have been observed in cases of very low E*, e.g. at E* = 1.87 (cf. Fig. 6, right).

During HIP, the microstructure of the specimens is transferred to a basket-weave α + β microstructure with starting globularization, as can be seen in Fig. 7. Again, the change in E* does not result in a noticeable change in the microstructure.

Some microporosity (pores in the size of 1–2 µm in diameter) seems to persist even after HIP. Most likely, the lack of fusion pores have been compacted but not completely closed during the HIP process, which becomes visible only in such high magnification.

3.5. Residual stress

Regarding the development of residual stresses with increasing scan speed, the results are presented in Fig. 8. The mean value of the cantilever beam deflection was Δh = 1.94 mm for the reference parameter

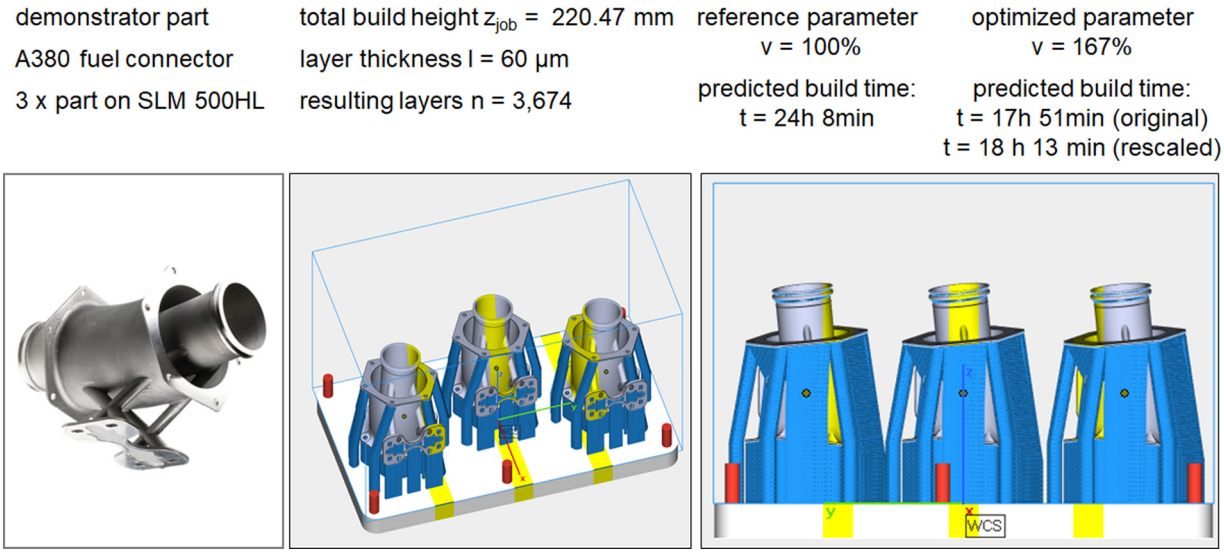

Fig. 10. Resulting productivity increase of 24.5 % through high-speed printing at ρ > 95 % on a demonstrator build job consisting of three scaled A380 fuel connectors.

set (v = 100 %). A moderate increase in the cantilever beam deflection with increasing scan speed was observed, and with the speed-optimized parameter set (v = 167 %) the mean value reached Δh = 2.25 mm. This increase corresponds to 15.8 %, and the trend appears to be rather linear.

4. Discussion

The experimental investigations have shown that, if an as-build density as low as ρ > 95 % is allowed, the normalized energy density and the normalized hatch may be varied in a much wider range than in the case of a ρ > 99.5 % requirement. As a result, the initial process map shown in Fig. 1 can now be updated with the data from the high-speed investigations (cf. Section 3), and is presented in Fig. 9.

The process window for the regular L-PBF process (without HIP) is characterized by the sum of all data sets plotted into Fig. 9 with a density ρ > 99.5 %, which is visualized as the green-coloured area. It narrows with smaller 1/h*. Therefore, a robust process will rather be achieved for 1/h* > 0.4. At 1/h* = 0.42, for example, E* may vary between 2.87 … 4.3. For the proposed combination of L-PBF with subsequent HIP, the as-build density required is lower (ρ > 95 %). The process window for this combination is visualized as the light-yellow area in Fig. 9, which is considerably broader.

There are many options to make use of the enlarged process window through the L-PBF and HIP combination, e.g. higher robustness against local or global process parameter deviations and thus higher quality. Also, the required laser power may be reduced. The most obvious, however, is the potential to increase the productivity by increasing the scan speed during L-PBF. Within the investigations presented here, the allowable scan speed increase was 60–70 % when compared to the reference.

To evaluate the effect of increasing scan speed on actual productivity, a demonstrator build job consisting of three Airbus A380 fuel connector parts was considered (cf. Fig. 10, for more information on the A380 fuel connector case study, please cf. to [45]). The parts were scaled to a build height of approximately 220 mm for this comparison, resulting in n = 3674 layers of l = 60 µm. Firstly, the reference parameter set (v = 100 %) was attributed to the demonstrator build job and transferred to the SLM 500 H L L-PBF machine. The predicted build time is t = 24 h and 8 min. Secondly, the high-speed parameter set (v = 167 %) was attributed to the build job. Again, the job was transferred to the L-PBF system, resulting in a predicted build time of t = 17 h and 51 min. A considerable amount of build time of 6 h and 17 min can be saved, corresponding to a productivity increase of approximately 26 %. Note that to compensate for the expected compaction of 2.1 % during HIP (cf. Fig. 5, center), the build job would need to be rescaled beforehand. This would increase the build time to 18 h and 13 min, leaving a net productivity increase of roughly 24.5 %.

5. Conclusion

Specimens manufactured from Ti-6Al-4V in two commercial L-PBF systems have been analyzed for density. A process map based on the method of Thomas et al. [27] and Wang et al. [26] was drawn from the data. In this approach, the density is plotted by the reciprocal normalized hatch 1/h* and a normalized energy density E*, and for the latter the term was refined by adding the heat of fusion. It could be shown that specimens with similar E* and 1/h* from both systems yielded comparable density values. The process map approach can therefore be considered as a valuable tool to define process windows and to transfer parameter sets from one L-PBF system to another.

In an attempt to increase productivity, the scan speed was increased and specimens with a reduced density have been produced intentionally until a threshold of ρ = 95 % was reached. It was shown that with the acceptance of up to 5 % porosity, the scan speed can be increased by around 2/3 compared to the reference. A slight increase in residual stresses was observed (cantilever deflection Δh = +15.8 %), probably due to even higher cooling rates. However, this aspect will need further research as it is contradictive to the observation made by Munsch [40]. The microstructure of the high-speed specimens did not show significant differences to the reference and consisted mainly of α' martensite, which is typical for L-PBF of this material [19]. Using HIP, both the reference as well as the high-speed specimens could be densified to ρ > 99.8 %.

Thus, a combination of L-PBF and subsequent HIP is proposed to enlarge the process window. This can be used for a variety of purposes such as higher reliability and quality or a lower required laser power and thus reduced investment costs. Other optimizations, e.g. for surface quality, may also be performed, possibly finding new global optima. The most obvious use, however, is to increase the scan speed and thus the productivity of the L-PBF process itself. The newly derived process parameters were attributed to a demonstrator build job, where the scan speed increase translated into an overall build time reduction of approximately 24.5 %. A careful case-by-case evaluaition is needed to see if this exceeds extra costs and time associated with the HIP process. Immediate advantage may be gained for parts that are currently manufactured to full density in L-PBF, and sent to HIP anyway. Also, the combination of HIP with heat-treatment that has lately been reported [46] will be in a favor of the combined approach presented here. The approach was validated for a layer thickness of l = 60 µm, but could well be transferred to higher layer thicknesses in future work, in order to further increase productivity if a lower accuracy is acceptable.

CRediT authorship contribution statement

Dirk Herzog: Conceptualization, Methodology, Investigation, Writing - original draft. **Katharina Bartsch:** Conceptualization, Writing - review & editing. **Bastian Bossen:** Investigation, Writing - review & editing.

Declaration of Competing Interest

The authors declare that they have no known competing financial interests or personal relationships that could have appeared to influence the work reported in this paper.

Acknowledgments

The authors would like to thank Laurenz Plöchl, Johannes Gårdstam and Jim Shipley of Quintus Technologies AB for conducting the Hot Isostatic Pressing (HIP), as well as for their invaluable contribution on the discussions of the HIP process requirements and parameters.

References

[1] D. Herzog, V. Seyda, E. Wycisk, C. Emmelmann, Additive manufacturing of metals, Acta Mater. 117 (2016) 371–392, https://doi.org/10.1016/j.actamat.2016.07.019.
[2] B. Dutta, S. Babu, B. Jared, Chapter 3 - Comparison of various additive manufacturing technologies, in: B. Dutta, S. Babu, B. Jared (Eds.), Science, Technology and Applications of Metals in Additive Manufacturing, Elsevier, Amsterdam, 2019, pp. 55–76.
[3] L. Gasman, 15 - Additive aerospace considered as a business, in: F.H. Froes, R. Boyer (Eds.), Additive Manufacturing for the Aerospace Industry, Elsevier, 2019, pp. 327–340.
[4] M. Brandt, The role of lasers in additive manufacturing, in: M. Brandt (Ed.), Laser Additive Manufacturing: Materials, Design, Technologies, and Applications, Woodhead Publishing, Duxford, 2017, pp. 1–18.
[5] D. Buchbinder, H. Schleifenbaum, S. Heidrich, W. Meiners, J. Bültmann, High power selective laser melting (HP SLM) of aluminum parts, Phys. Procedia 12 (2011) 271–278, https://doi.org/10.1016/j.phpro.2011.03.035.
[6] N.N, Material Data Sheet EOS Titanium Ti64 M290 (accessed 17 January 2020), https://cdn.eos.info/a4eeb73865d54434/5926811b3739/Ti-Ti64_9011-0014_9011-0039_M290_Material_data_sheet_11-17_en.pdf.
[7] S.E. Brika, M. Letenneur, C.A. Dion, V. Brailovski, Influence of particle morphology and size distribution on the powder flowability and laser powder bed fusion manufacturability of Ti-6Al-4V alloy, Addit. Manuf. 31 (2020), https://doi.org/10.

1016/j.addma.2019.100929 100929.
[8] X. Shi, S. Ma, C. Liu, C. Chen, Q. Wu, X. Chen, J. Lu, Performance of high layer thickness in selective laser melting of Ti6Al4V, Materials (Basel) 9 (2016), https://doi.org/10.3390/ma9120975.
[9] F. Cabanettes, A. Joubert, G. Chardon, V. Dumas, J. Rech, C. Grosjean, Z. Dimkovski, Topography of as built surfaces generated in metal additive manufacturing: a multi scale analysis from form to roughness, Precis. Eng. 52 (2018) 249–265, https://doi.org/10.1016/j.precisioneng.2018.01.002.
[10] N.N, Laser Beam Powder Bed Fusion: Technology Deep Dive, (2019) https://additive-manufacturing-report.com/technology/laser-beam-powder-bed-fusion/.
[11] M. Munsch, M. Schmidt-Lehr, E. Wycisk, Metal Additive Manufacturing: Report 2019, 1st edition, Ampower GmbH & Co. KG, Hamburg, 2019.
[12] S. Bremen, W. Meiners, A. Diatlov, Selective laser melting, LTJ 9 (2012) 33–38, https://doi.org/10.1002/latj.201290018.
[13] H. Schleifenbaum, W. Meiners, K. Wissenbach, C. Hinke, Individualized production by means of high power Selective Laser Melting, CIRP J. Manuf. Sci. Technol. 2 (2010) 161–169, https://doi.org/10.1016/j.cirpj.2010.03.005.
[14] R. Poprawe, C. Hinke, W. Meiners, J. Schrage, S. Bremen, S. Merkt, SLM production systems: recent developments in process development, machine concepts and component design, in: C. Brecher (Ed.), Advances in Production Technology, Springer Open, Cham, 2015, p. 57.
[15] A. Wiesner, D. Schwarze, Multi-laser selective laser melting, Proceedings of the 8th International Conference on Photonic Technologies LANE, Bayerisches Laserzentrum GmbH, 2014.
[16] R. Kopf, J. Gottwald, A. Jacob, M. Brandt, G. Lanza, Cost-oriented planning of equipment for selective laser melting (SLM) in production lines, CIRP Ann. 67 (2018) 471–474, https://doi.org/10.1016/j.cirp.2018.04.032.
[17] M. Peters, J. Hemptenmacher, J. Kumpert, C. Leyens, Structure and properties of titanium and titanium alloys, Titanium and Titanium Alloys: Fundamentals and Applications, Wiley-VCH, Weinheim, 2003, pp. 1–36.
[18] C. Emmelmann, P. Scheinemann, M. Munsch, V. Seyda, Laser additive manufacturing of modified implant surfaces with osseointegrative characteristics, Phys. Procedia 12 (2011) 375–384, https://doi.org/10.1016/j.phpro.2011.03.048.
[19] L. Thijs, F. Verhaeghe, T. Craeghs, J. van Humbeeck, J.-P. Kruth, A study of the microstructural evolution during selective laser melting of Ti–6Al–4V, Acta Mater. 58 (2010) 3303–3312, https://doi.org/10.1016/j.actamat.2010.02.004.
[20] H.K. Rafi, N.V. Karthik, H. Gong, T.L. Starr, B.E. Stucker, Microstructures and Mechanical Properties of Ti6Al4V Parts Fabricated by Selective Laser Melting and Electron Beam Melting, J. Mater. Eng. Perform. 22 (2013) 3872–3883, https://doi.org/10.1007/s11665-013-0658-0.
[21] T. Vilaro, C. Colin, J.D. Bartout, As-fabricated and heat-treated microstructures of the Ti-6Al-4V alloy processed by selective laser melting, Metall. Mat. Trans. A 42 (2011) 3190–3199, https://doi.org/10.1007/s11661-011-0731-y.
[22] J.L. Bartlett, B.P. Croom, J. Burdick, D. Henkel, X. Li, Revealing mechanisms of residual stress development in additive manufacturing via digital image correlation, Addit. Manuf. 22 (2018) 1–12, https://doi.org/10.1016/j.addma.2018.04.025.
[23] J.L. Bartlett, X. Li, An overview of residual stresses in metal powder bed fusion, Addit. Manuf. 27 (2019) 131–149, https://doi.org/10.1016/j.addma.2019.02.020.
[24] E. Wycisk, S. Siddique, D. Herzog, F. Walther, C. Emmelmann, Fatigue performance of laser additive manufactured Ti–6Al–4V in very high cycle fatigue regime up to 109 cycles, Front. Mater. 2 (2015) 72, https://doi.org/10.3389/fmats.2015.00072.
[25] A. Khorasani, I. Gibson, M. Goldberg, G. Littlefair, On the role of different annealing heat treatments on mechanical properties and microstructure of selective laser melted and conventional wrought Ti-6Al-4V, Rapid Prototyp. J. 23 (2017) 295–304, https://doi.org/10.1108/RPJ-02-2016-0022.
[26] Y. Wang, C. Kamath, T. Voisin, Z. Li, A processing diagram for high-density Ti-6Al-4V by selective laser melting, Rapid Prototyp. J. 24 (2018) 1469–1478, https://doi.org/10.1108/RPJ-11-2017-0228.
[27] M. Thomas, G.J. Baxter, I. Todd, Normalised model-based processing diagrams for additive layer manufacture of engineering alloys, Acta Mater. 108 (2016) 26–35, https://doi.org/10.1016/j.actamat.2016.02.025.
[28] T. Voisin, N.P. Calta, S.A. Khairallah, J.-B. Forien, L. Balogh, R.W. Cunningham, A.D. Rollett, Y.M. Wang, Defects-dictated tensile properties of selective laser melted Ti-6Al-4V, Mater. Des. 158 (2018) 113–126, https://doi.org/10.1016/j.matdes.2018.08.004.
[29] Q.C. Liu, J. Elambasseril, S.J. Sun, M. Leary, M. Brandt, P.K. Sharp, The effect of manufacturing defects on the fatigue behaviour of Ti-6Al-4V specimens fabricated using selective laser melting, 11th International Fatigue Congress, Trans Tech Publications, Durnten-Zurich, Switzerland, 2014, pp. 1519–1524.
[30] C. Qiu, N.J.E. Adkins, M.M. Attallah, Microstructure and tensile properties of selectively laser-melted and of HIPed laser-melted Ti–6Al–4V, Mater. Sci. Eng. A 578 (2013) 230–239, https://doi.org/10.1016/j.msea.2013.04.099.
[31] H.V. Atkinson, S. Davies, Fundamental aspects of hot isostatic pressing: an overview, Metall. Mat. Trans. A 31 (2000) 2981–3000, https://doi.org/10.1007/s11661-000-0078-2.
[32] H. Masuo, Y. Tanaka, S. Morokoshi, H. Yagura, T. Uchida, Y. Yamamoto, Y. Murakami, Effects of defects, surface roughness and HIP on fatigue strength of Ti-6Al-4V manufactured by additive manufacturing, Procedia Struct. Integr. 7 (2017) 19–26, https://doi.org/10.1016/j.prostr.2017.11.055.
[33] M. Qian, W. Xu, M. Brandt, H.P. Tang, Additive manufacturing and postprocessing of Ti-6Al-4V for superior mechanical properties, MRS Bull. 41 (2016) 775–784, https://doi.org/10.1557/mrs.2016.215.
[34] H.V. Atkinson, S. Davies, Fundamental aspects of hot isostatic pressing: an overview, Metall. Mater. Trans. A 31 (2000) 2981–3000, https://doi.org/10.1007/s11661-000-0078-2.
[35] A. Eklund, M. Ahlfors, F. Bahbou, J. Wedenstrand, Optimizing HIP and printing parameters for EBM Ti-6Al-4V, KEM 770 (2018) 174–178, https://doi.org/10.4028/www.scientific.net/KEM.770.174.
[36] N.L. Loh, K.Y. Sia, An overview of hot isostatic pressing, J. Mater. Process. Technol. 30 (1992) 45–65, https://doi.org/10.1016/0924-0136(92)90038-T.
[37] S. Das, N. Harlan, J.J. Beaman, D.L. Bourell, Selective laser sintering of high performance high temperature materials, International Solid Freeform Fabrication Symposium (1996).
[38] C. Qiu, N.J.E. Adkins, H. Hassanin, M.M. Attallah, K. Essa, In-situ shelling via selective laser melting: modelling and microstructural characterisation, Mater. Des. 87 (2015) 845–853, https://doi.org/10.1016/j.matdes.2015.08.091.
[39] C. Cai, X. Gao, Q. Teng, M. Li, K. Pan, B. Song, C. Yan, Q. Wei, Y. Shi, A novel hybrid selective laser melting/hot isostatic pressing of near-net shaped Ti-6Al-4V alloy using an in-situ tooling: interfacial microstructure evolution and enhanced mechanical properties, Mater. Sci. Eng. A 717 (2018) 95–104, https://doi.org/10.1016/j.msea.2018.01.079.
[40] M. Munsch, Reduzierung von Eigenspannungen und Verzug in der laseradditiven Fertigung, first ed., Cuvillier Verlag, Göttingen, 2013.
[41] R. Boyer, G. Welsch, E.W. Collings, Materials Properties Handbook: Titanium Alloys, ASM International, Materials Park, Ohio, 1994 p. 516.
[42] M. Boivineau, C. Cagran, D. Doytier, V. Eyraud, M.-H. Nadal, B. Wilthan, G. Pottlacher, Thermophysical properties of solid and liquid Ti-6Al-4V (TA6V) alloy, Int. J. Thermophys. 27 (2006) 507–529, https://doi.org/10.1007/PL00021868.
[43] J.R. Davis, Metals Handbook - Properties and Selection: Nonferrous Alloys and Special-Purpose Materials, [tenth. ed.], sixth. print ASM International, Materials Park, Ohio, 2000.
[44] A.B. Spierings, M. Schneider, R. Eggenberger, Comparison of density measurement techniques for additive manufactured metallic parts, Rapid Prototyp. J. 17 (2011) 380–386, https://doi.org/10.1108/13552541111156504.
[45] S. Asche, Schnelle Wege in Den 3-D-Druck, (2019) (accessed 24 March 2020), https://www.vdi-nachrichten.com/technik/schnelle-wege-in-den-3-d-druck/.
[46] M. Ahlfors, High Pressure Heat Treatment of AM Parts - Combining HIP and Heat Treatment, Västerås, (2019).